Biosensing with a Graphene-Based FET

C.R. Tamanaha,[1] R. Stine,[2] J.T. Robinson,[3] M. Baraket,[4] S.P. Mulvaney,[1] S.G. Walton,[5] and P.E. Sheehan[1]
[1]*Chemistry Division*
[2]*Nova Research, Inc.*
[3]*Electronics Science and Technology Division*
[4]*National Research Council Postdoctoral Research Associate (formerly)*
[5]*Plasma Physics Division*

Introduction: A low-cost sensor that continuously and rapidly looks for a range of biomolecules is a longstanding goal for the biosensor community that remains unfulfilled. Such real-time sensors could lead to "more effective point of injury care for Sailors and Marines," and "enhanced health and warfighter performance both afloat and ashore."[1]

The arduous quest for such an "ultimate" biosensor, one that fully meets the Office of Naval Research (ONR) vision of enhancing warfighter health and survivability, has spanned nearly 50 years. One particular application of such a sensor, medical diagnostics, utilizes biosensor technologies based on nucleic acid and immunoassays. Most of these biosensor technologies currently use a label to facilitate detection. A label can be a fluorescent molecule or a magnetic bead or any component that helps signal the presence of the target biomolecule. In particular, fluorescence labels remain the predominant strategy because of their signal strength, availability of multiple emission wavelengths, and their compatibility with multiplexed, high-throughput, in situ and in vivo applications. The difficulty is that labels introduce complexity into the sensor system and, in the case of fluorescence labels, are consumed, whereby detection can only last a defined duration. In contrast, "label-free sensing" eliminates sample handling to attach the label to the target and alleviates steric hindrance, thus resulting in higher sensitivity, faster response, and ultimately lower costs.

A popular approach for label-free sensing is based on the field effect transistor (FET), which consists of two terminals, the source and drain, and a gate that controls the resistance of the device (Fig. 1, top). For sensor applications, the gate terminal is replaced by a material that can sense biomolecules. Typically, it consists of covalently bound "probe" biomolecules that can capture the target biomolecule via biological interactions such as protein–ligand and DNA hybridization. We refer to these modified structures as biologically active field effect transistors, or BioFETs (Fig. 1, bottom). Several promising biosensing advances have used nanoscale one-dimensional materials such as carbon nanotubes as the gate.[2] Recently, we demonstrated that an ideal gate material for BioFETs is chemically modified graphene (CMG).[3] Because graphene is only one atom thick, the highly mobile electrons at or near its surface are extremely sensitive to local charge changes. Because most biomolecules are charged, their binding to a graphene-based gate will disrupt the flow of the electrons. Of course, this only works if the graphene is properly biofunctionalized such that protein–ligand interactions or nucleic acid hybridization can occur.

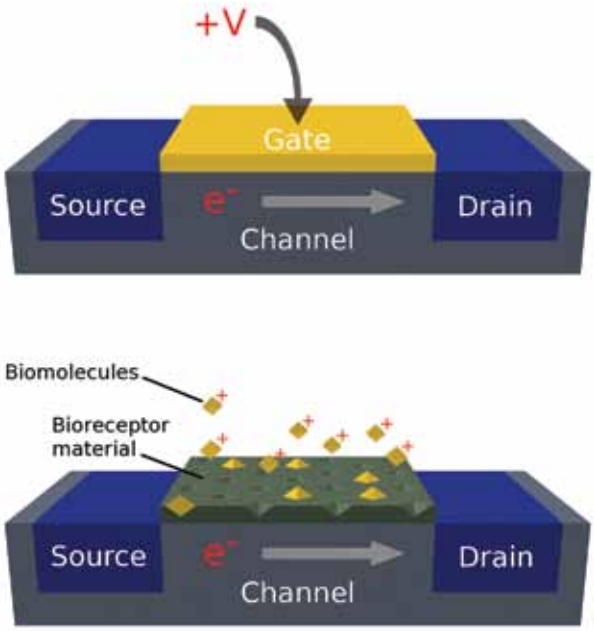

FIGURE 1
BioFET concept. The gate electrode of a standard FET (top) is replaced by biological components (bottom). Changes in charge distribution at the gate, due to biomolecular recognition activity, modulate current transport through the semiconductor.

Graphene Biofunctionalization: Unfortunately, pristine graphene is inert, and chemical sites to which biomolecules can be easily covalently tethered must be carefully created. We have pursued two independent pathways: (1) the modification of reduced graphene oxide (rGO), and (2) the implantation of chemical attachment sites into chemical vapor deposition (CVD)-grown graphene sheets via ultra-low-temperature gas plasmas.

In the first pathway, graphite powder is converted to graphene oxide (GO) using strong oxidizers and sonication to produce a material rich with epoxyl, carboxyl, and hydroxyl groups, which are ideal for biofunctionalization. Unlike graphene, however, GO is electrically insulating, and the traditional method of using hydrazine reduction to restore conductivity strips the GO of these facile attachment points. Faced with the contradictory requirements to retain the oxide functional groups for biofunctionalization

and to remove them to regain conductivity, we found a breakthrough in the form of selective reduction of the GO material.[3] A placeholder molecule, the bifunctional cross-linker ethylenediamine (EDA), is reacted with GO's epoxide groups prior to reduction. The entire film is then reduced and the bound EDA survives the aggressive reduction process to leave behind a primary amine group, an ideal attachment site for coupling to DNA or proteins. This was the critical step because it resulted in a CMG that was both highly conductive and supported covalent attachment of biomolecules.

In the second pathway, graphene was produced by low-pressure (1 Torr) CVD on copper foils by the NRL Electronic Materials Branch and then transferred from the copper foil to silicon/SiO_2 substrates via wet etching. The material was then treated using an ammonia (NH_3)-containing plasma process developed in the NRL Plasma Physics Division.[4] As in the previous pathway, the end result is incorporation of primary amines in the CVD graphene sheet that can bind to DNA and proteins. The appeal of this second pathway is straightforward: the direct and controllable addition of chemical attachment points to pristine graphene. Such control over attachment point density has been shown to be critical in past efforts at developing biosensor chemistry. This is in sharp contrast to the first approach, which uses nonconductive GO, which, while cheaper to produce, has an abundance of defects that necessitate reduction to regain the conductivity required for biosensing.

Sensor Construction and Measurement: Graphene sheets are transferred over pre-patterned interdigitated gold electrodes on SiO_2 substrates. The sensing areas encompassing the electrodes are defined by photolithography, and excess graphene is removed via oxygen plasma etch. The non-sensing areas of the gold electrodes are protected by a layer of either Si_3N_4 or Al_2O_3. For the rGO BioFET, single-stranded DNA probes are covalently attached via the EDA pathway described above. For the CVD-grown graphene BioFET, primary amines are introduced by exposure to a low-pressure (75 mTorr) Ar/NH_3 plasma. For both types of sensors, primary amine terminated DNA is linked via glutaraldehyde to create probe spots. In each experiment, two BioFETs are operated simultaneously using a lock-in amplifier in a differential measurement scheme. One BioFET contains single-stranded DNA probes for a complementary single-stranded DNA target. The other BioFET acts as a reference with probes for a noncomplementary DNA target. Taking the difference of the signals from these two sensors results in specific binding signal only.

Performance: Figure 2 is a performance comparison of the BioFET sensors constructed by the two described methods. The sensors were exposed to 1 μM concentration of target and control DNA in a 15 mM phosphate-buffered saline solution. As can be seen, the CVD graphene functionalized with primary amines via controlled plasma exposure shows a 4 times larger signal-to-noise ratio compared to our rGO sensors. In addition, we showed the dose-dependent response on a set of rGO BioFET sensors to changes in complementary DNA concentrations between 1 μM and 10 nM with a projected 2 nM detection limit (Fig. 3).[3] More recently, improvements in electronic noise levels and rGO surface biofunctionalization chemistries have resulted in preliminary data indicating high pM sensitivity (unpublished data) — a result that begins to challenge traditional analytical techniques.

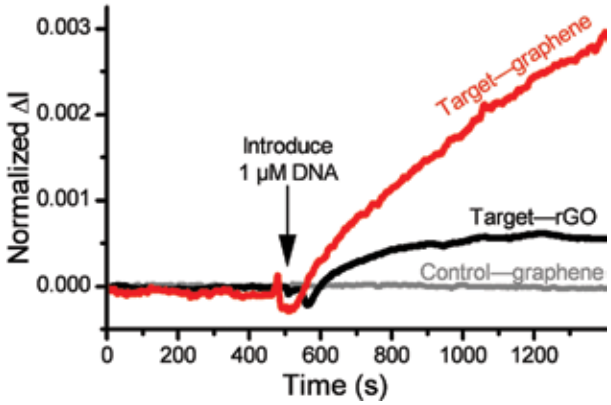

FIGURE 2
Response of aminated graphene DNA sensor to both target and control solutions. Target is complementary to probe; control is noncomplementary to probe. The sensing response is compared to that seen from a reduced graphene oxide (rGO) DNA sensor for an identical target solution. It shows an enhancement of the signal-to-noise ratio as compared to the rGO sensor.

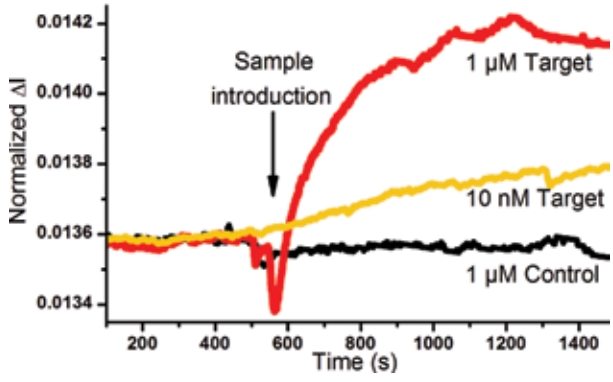

FIGURE 3
Unoptimized rGO-based dual BioFET DNA detection. Target is complementary to probe on biofunctionalized rGO; control is noncomplementary to probe. Signal is the difference between the reference BioFET and the DNA-functionalized BioFET.

Summary: We have developed chemical modification procedures on graphene for the attachment of biorecognition molecules (e.g., antibodies and DNA),

to achieve specific target binding and a signal response without the need for a label (e.g., optical or magnetic). The high electron mobility near or at the surface of graphene-based BioFETs gives these devices their high sensitivity. We have shown that modifying the graphene surfaces to accept biologically sensitive material with native charges that disrupt the flow of the FET's electrons is a winning strategy that has enormous potential for satisfying many of the criteria for an ideal biosensor: rapid, sensitive, label-free detection in an inexpensive, compact, low-power, electronically integrated module. The low inherent cost of these systems makes them especially appealing. Both CVD graphene and rGO are inexpensive to produce and can be transferred to low-cost flexible substrates such as plastics. Current efforts aim to produce such devices and to minimize steps requiring a clean room by using, for instance, ink jet printing to deposit electrodes and isolation layers.

Acknowledgments: We would like to acknowledge ONR, the NRL Institute for Nanoscience, and the Defense Threat Reduction Agency (DTRA) Joint Science and Technology Office for Chemical and Biological Defense (JST-CBD) for funding.

[Sponsored by ONR and DTRA JST-CBD]

References

[1] Naval S&T Strategic Plan, Office of Naval Research, Arlington, VA, Sept. 2011.

[2] X. Dong, C.M. Lau, A. Lohani, S.G. Mhaisalkar, J. Kasim, Z. Shen, X. Ho, J.A. Rogers, and L.-J. Li, "Electrical Detection of Femtomolar DNA via Gold-Nanoparticle Enhancement in Carbon-Nanotube-Network Field-Effect Transistors," *Adv. Mater.* **20**, 2389–2393 (2008).

[3] R. Stine, J.T. Robinson, P.E. Sheehan, and C.R. Tamanaha, "Real-time DNA Detection Using Reduced Graphene Oxide Field Effect Transistors," *Adv. Mater.* **22**, 5397–5300 (2010).

[4] S.G. Walton, E.H. Lock, M. Baraket, D.R. Boris, R.F. Fernsler, S.H. North, C.R. Taitt, J.T. Robinson, F.K. Perkins, and P.E. Sheehan,"Plasma Processing of Ion Energy-sensitive Materials," *2010 NRL Review* (Naval Research Laboratory, Washington, DC, 2011) pp. 187–189.

Silicon Spintronics at 500 K

C.H. Li, O.M.J. van 't Erve, and B.T. Jonker
Materials Science and Technology Division

Silicon Spintronics: The control of spin-polarized carrier populations and currents offers a new paradigm for information processing in semiconductors. The *International Technology Roadmap for Semiconductors*[1] has identified the electron's spin as a new state variable, a "spintronic" approach, to be explored beyond Moore's Law. Silicon (Si) is an ideal host for such a spin-based technology, because its low atomic mass and crystal inversion symmetry result in very small spin orbit interactions and long spin lifetimes.

Challenge: Although the steady reduction in device feature size predicted by Moore's Law has been remarkably successful, critical device dimensions now approach atomic length scales, so that further size scaling becomes untenable. Researchers have been forced to look beyond the simple reduction of size to develop future generations of electronic devices. Utilization of the electron's spin angular momentum as an alternate state variable provides additional functionality and performance for future electronic devices envisioned beyond the current roadmap. Electrical generation, manipulation, and detection of significant spin polarization in silicon at temperatures that meet commercial and military requirements are essential to validate spin as an alternative to charge for a device technology beyond Moore's Law.

Spin Accumulation in Si to 500 K: To make a semiconductor spintronic device, one needs contacts that can both generate a current of spin-polarized electrons (spin injector), and detect the spin polarization of the electrons (spin detector) in the semiconductor.[2] A material with a spin-polarized density of states such as a ferromagnetic (FM) metal is often used. A thin layer (~2 nm) of silicon dioxide (SiO_2), a key element of the vast Si electronics industry because it is easy to form and produces an electrically stable self-interface with the low interface state density necessary for device operation, is placed between the ferromagnetic contact and Si to serve as a tunnel barrier. This facilitates spin injection by controlling the series resistance, and prevents intermixing between the ferromagnet and Si.

We probe the spin environment directly under the ferromagnet/SiO_2 contact using the three-terminal geometry shown in Fig. 4. In this geometry, a spin-polarized current is injected from contact 2 to 1, and a voltage is measured across contacts 2 and 3. Electrical spin injection produces spin accumulation in the transport channel under magnetic contact 2 and a corresponding output voltage. When a magnetic field B_Z is applied, the injected spins precess and dephase, and the spin accumulation decreases to zero. This Hanle effect is conclusive evidence of spin accumulation, and allows a direct measure of the spin lifetime and, subsequently, spin diffusion length, critical parameters for device operation. As shown in Fig. 5, we clearly observe Hanle precession of the electron spin accumulation in the Si channel under the contact over a wide range of temperatures up to 500 K.

Spin Lifetimes and Diffusion Lengths: The lineshape of the three-terminal Hanle data can be fit to ob-

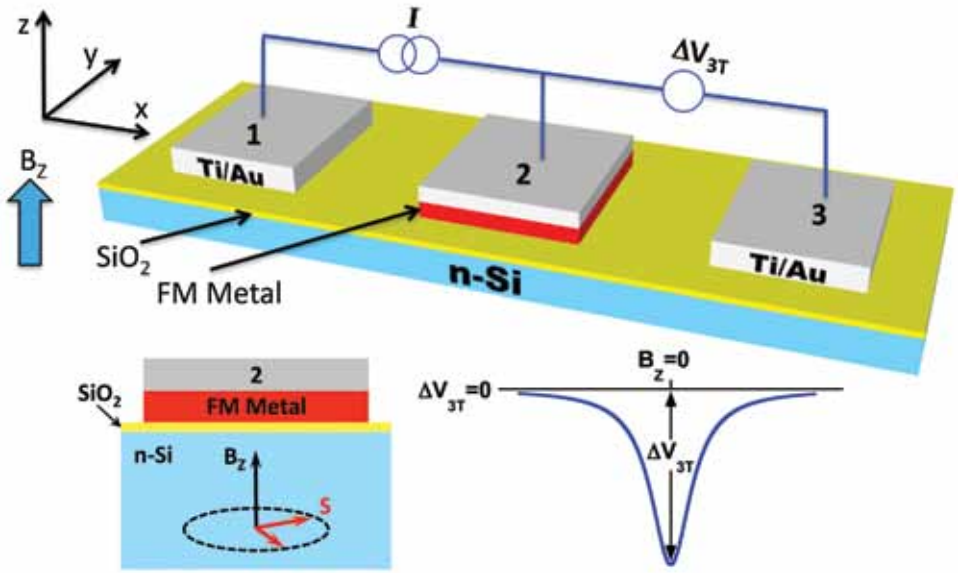

FIGURE 4
Schematic diagram of the three-terminal measurement geometry, where a current is applied to contacts 2 and 1, and a voltage is measured across contacts 2 and 3. Electrical spin injection produces spin accumulation in the transport channel under magnetic contact 2 and a corresponding output voltage ΔV_{3T}. When a magnetic field B_Z is applied, the injected spins precess and dephase, and $\Delta V_{3T}(B_Z)$ decreases to zero.

tain a value for the spin lifetime by using a Lorentzian expression analogous to the classic optical Hanle effect. Such fits yield a spin lifetime of 100 ps for the sample shown in Fig. 4 at 300 K. This lifetime is about 10 times shorter than predicted by theory for bulk Si of the same carrier concentration. This may be a consequence of the fact that the Lorentzian fitting procedure produces a lower bound for the lifetime, but is also a trend we have observed previously and attributed to the vicinity of the contact interface, where both the reduced symmetry and surface/impurity scattering are likely to produce more rapid spin relaxation than in the bulk. The spin lifetimes extracted in this three-terminal geometry therefore reflect the environment close to the contact, relevant for actual device operation.

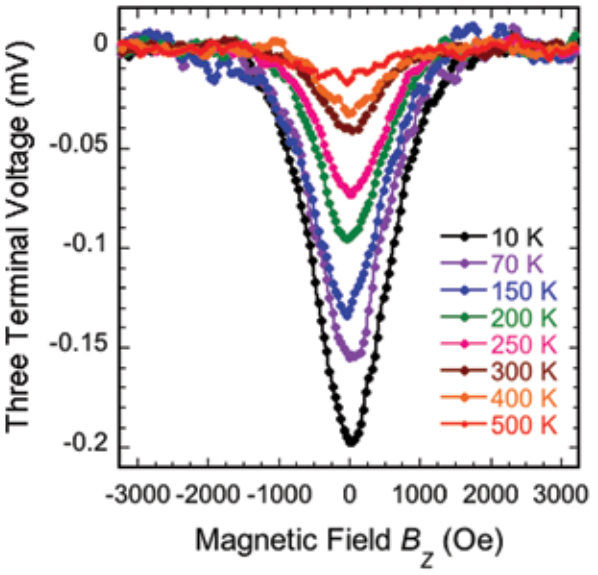

FIGURE 5
Three-terminal Hanle curves for a Si sample doped at 3×10^{19}/cm^3 at temperatures from 10 to 500 K, with an injection current of 500 μA and voltage of 1 V.

The spin diffusion length can also be calculated from the spin lifetime and the diffusion constant derived from the measured carrier concentration and mobility. We obtain a value of 190 nm for the sample with a carrier concentration of 3×10^{19}/cm^3, and ~400 nm for a lower doped sample (3×10^{18}/cm^3) near room temperature and above, demonstrating that practical devices based on spin transport in Si are viable with conventional lithographic and fabrication techniques found in most Si fabrication lines.

Dependence of Spin Lifetime on Electron Density: To verify that the origin of the measured spin accumulation is indeed from the semiconductor channel and not interfacial states, we fabricate devices on Si samples with a range of carrier concentrations and measure the corresponding spin lifetimes, as shown in Fig. 6. Each data point plotted represents a separate device on which many measurements were made. The decrease in spin lifetime with increasing carrier concentration is consistent with the electron spin resonance results for bulk Si, and attributed to impurity-dominated Elliot–Yafet spin relaxation processes. The

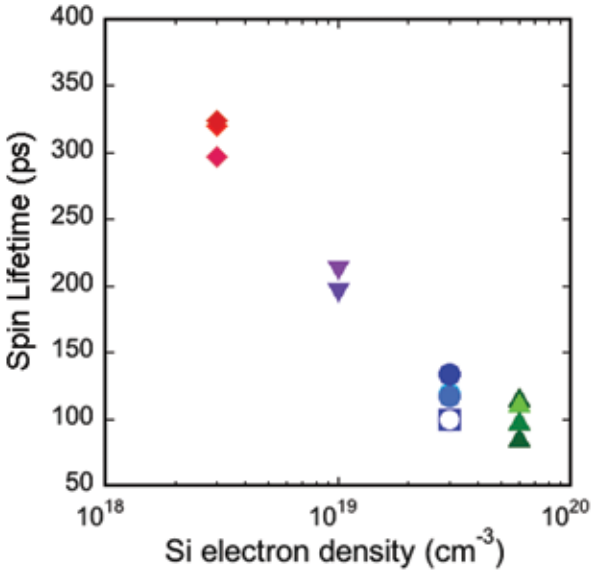

FIGURE 6
Spin lifetime as a function of the Si electron density at 10 K. The symbols distinguish the ferromagnetic metal used: solid symbols correspond to devices with $Ni_{0.8}Fe_{0.2}$ contacts, while open symbols correspond to $Co_{0.9}Fe_{0.1}$ contacts.

fact that the spin lifetime exhibits a clear dependence on the Si carrier density provides clear evidence that the spin accumulation/precession indeed occurs in the Si channel rather than in localized interface states, a key issue for spin transport in semiconductors. This breakthrough overcomes a major obstacle in achieving spin manipulation at temperatures well above the requirements of commercial (85 °C), industrial (100 °C), and military (125 °C) applications in the most widely used semiconductor, and is a major enabling step toward the realization of Si-based spintronic devices.[3]

[Sponsored by ONR and the NRL Base Program (CNR funded)]

References

[1] International Technology Roadmap for Semiconductors, www.itrs.net (2009).
[2] O.M.J. van 't Erve, A.T. Hanbicki, M. Holub, C.H. Li, C. Awo-Affouda, P.E. Thompson, and B.T. Jonker, "Electrical Injection and Detection of Spin-Polarized Carriers in Silicon in a Lateral Transport Geometry," *Appl. Phys. Lett.* **91**, 212109 (2007).
[3] C.H. Li, O.M.J. van 't Erve, and B.T. Jonker, "Electrical Injection and Detection of Spin Accumulation in Silicon to 500 K with Magnetic Metal/Silicon Dioxide Contacts," *Nature Communications* **2**, 245 (2011).

Poro-Vascular Composites

J.P. Thomas,[1] M.H. Merrill,[1] K.M. Metkus,[2] A. Piqué,[1] and R.K. Everett[1]
[1] *Materials Science and Technology Division*
[2] *NOVA Research, Inc.*

Introduction: We are developing a new class of multifunctional composites with controllable surface morphology. These are two-phase (solid-fluid), thin, flexible, skinlike laminates with surface "pore" arrays that are connected to an internal vascular network. They have both structural (skin) and surface (morphology control) functionality and are called poro-vascular (PV) composites.

The solid phase of the PV composite is a laser micromachined polyimide layer. It incorporates an ionic liquid (IL) phase whose height and meniscus shape within the pores can be controlled to vary the mesoscale surface morphology from dimples to domes (see Fig. 7). ILs are neutral mixtures of charged (+ and –) molecular species with low enough vapor pressure to be considered nonevaporating. Fluid height and meniscus shape control are achieved through volumetric pumping within the vascular network and electrical polarization for contact angle control on the pore and exterior surfaces via electrowetting-on-dielectric (EWOD).[1]

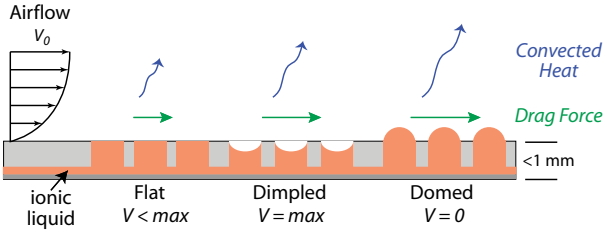

FIGURE 7
Schematic of PV composite surface morphologies for active control of aerodynamic (skin-friction) drag and laminar-to-turbulent transition.

Our research has focused on understanding how the IL composition and electrode configuration (layer compositions and thicknesses) influence contact angle control via EWOD; prototype development for wind-tunnel testing (to determine range of drag control); and computational modeling of the effects of surface morphology (pore diameter, spacing, and arrangements) on skin-friction drag and on the transition from laminar to turbulent boundary layer flow.

Application: Aerodynamic drag is comprised of skin-friction and form (or pressure) components. Drag forces can lead to a significant waste of energy in mobility applications. For a vehicle to maintain a steady-state velocity in an air environment, the vehicle's propulsion system must supply power equal to the drag force times the vehicle velocity. Technologies that can reduce and control drag offer opportunities for improving vehicle energy efficiencies and performance. PV composites with reconfigurable surface morphology will allow for new modes of air-vehicle maneuver con-

trol via changes in skin-friction drag and for control of the laminar-to-turbulent transition point on airfoils to achieve reduction in form drag that will increase flight efficiency.[2]

Fabrication and EWOD Experiments: PV composite test samples and prototypes are being fabricated using pulsed UV laser micromachining to create arbitrary shaped pores, various pore arrays, and different sized (width and depth) vascular trenches or channels in a variety of polyimide and polyetherimide materials (Fig. 8). The laser spot-size can be controlled to achieve machined features as small as 10 μm.

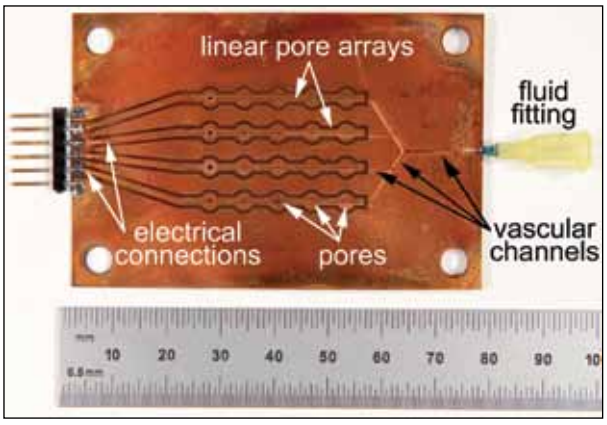

FIGURE 8
Early PV composite prototype (75 × 50 mm) used for fluidic control testing. This prototype uses an external displacement pump for fluid height control.

EWOD control of IL contact angle within the pores and on the surface of the PV composite is achieved by applying a thin metal coating or using an intrinsically conductive polyimide pore layer as an electrode. The conductive electrode is electrically insulated by a vapor-deposited Parylene polymer dielectric coating on which a thin layer of Teflon AF is applied to create an intrinsically "nonwetting" (hydrophobic) surface. Small amounts of liquid on the hydrophobic surface collect as spherical drops (lotus-leaf effect) with contact angles greater than 90°. The application of an electric potential between an electrode in the IL and the insulated electrode on the PV composite surface/pores reduces the IL contact angle to less than 90°. This corresponds to a "wetting" state with liquid drops tending to spread out over the surface.

Flat test samples have been used for characterizing IL and electrode effects on EWOD. For example, contact angle vs applied potential has been measured for a 1-ethyl-3-methylimidazolium methyl sulfate IL from 0 to ±200 V in 10 V steps on Kapton HN films coated with 150 nm of gold, 5 μm Parylene-HT, and 40 or 185 nm of Teflon AF 1600. Figure 9 shows how the contact angle changes with applied potential in comparison with the theoretically predicted (Lippmann–Young) curve. At zero applied voltage, the contact angle is 98° ± 6°. The positive and negative applied voltage behaviors are roughly similar, with a 20° to 24° decrease in contact angle; hysteresis between the initial and final

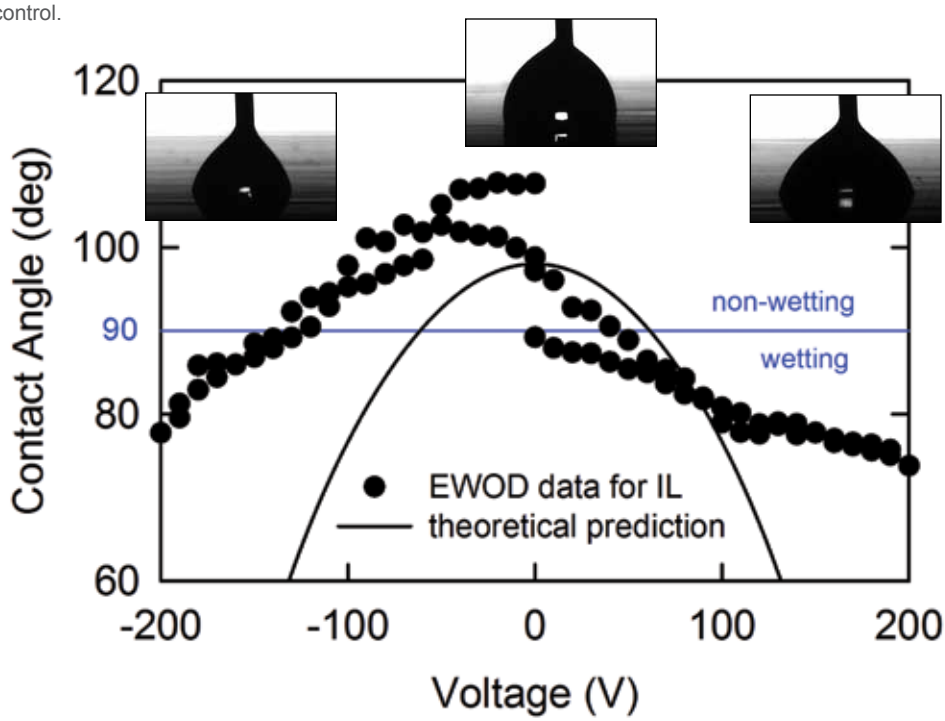

FIGURE 9
EWOD results for a 1-ethyl-3-methylimidazolium methyl sulfate IL. All points are averages of multiple measurements. The theoretically predicted (Lippmann–Young) curve is shown for comparison. Insets show the IL drop and contact angle at –200, 0, and 200 V.

contact angles is less than 9°. Repeating the same experiments with an aqueous (ideal) solution of 0.1 M NaCl results in an initial contact angle of 118° ± 5° and a total change of nearly 40°. Our findings agree with other researchers who have also reported less efficient EWOD control with ILs.[3] The observed difference is hypothesized to be due to interactions between the electrode surface morphology and chemistry and the IL. Ongoing studies using films with different electrodes and Parylene types (roughness) but identical surface chemistry (Teflon AF 1600) are exploring this important phenomenology as well as seeking electrode configurations that achieve maximal changes in contact angle vs applied potential.

Future plans include fabricating fully functional prototypes for wind-tunnel testing of skin-friction and form drag control after the EWOD experiments above identify one or more optimal electroding configurations.

[Sponsored by the NRL Base Program (CNR funded)]

References

[1] F. Mugele and J.-C. Baret, "Electrowetting: from Basics to Applications," *J. Phys. Condens. Matter* **17**, R705–R774 (2005).

[2] J.P. Thomas, M.H. Merrill, K.M. Metkus, A. Piqué, and R.K. Everett, "Multifunctional Composites with Applications to Energy Performance and Efficiency," paper AF1438, ICCM18: The 18th International Conference on Composite Materials, Jeju, Korea, August 2011.

[3] M. Paneru, C. Priest, R. Sedev, and J. Ralston, "Static and Dynamic Electrowetting of an Ionic Liquid in a Solid/Liquid/Liquid System," *J. Am. Chem. Soc.* **132**, 8301–8308 (2010).

Low-Cost Processing of Titanium and its Alloys

A.W. Fliflet,[1] M.A. Imam,[2] and R.K. Everett[2]
[1] *Plasma Physics Division*
[2] *Materials Science and Technology Division*

Microwave Sintering of Metal Powders: Titanium (Ti) has many attractive attributes for Naval applications, including high specific strength, no magnetic signature, and excellent corrosion resistance. However, its use has been limited by high processing costs. In the past few years, the availability of titanium powders, produced by a number of novel processes, has resulted in broad interest in using these lower cost materials for military, industrial, and aerospace applications. Powder metallurgy is an effective, cost-reducing way to produce high-quality, near-net-shape products by sintering at a fraction of the cost of melting and casting. Traditionally, sintering is performed in a conventional vacuum furnace and overall processing times can be many hours to days.

The Naval Research Laboratory has been investigating the use of microwave and millimeter-wave systems in material processing for more than a decade.[1] Typically, microwave processing improves energy efficiency by direct heating of the work piece via in-depth energy deposition. The in-depth heating permits very rapid processing (cycle times of less than 10 minutes), which is intended to preserve a very fine grain structure in the final product. The fine grain size obtained can lead to excellent mechanical properties and to the possibility of superplastic forming of such materials to net shape components. Generally, the direct heating of metals by microwaves is not effective, due to the high conductivity of the metal surface. This is not the case with powder metal compacts that are not fully dense. These should be more properly treated as artificial dielectrics — a composite of the metal powder and gas/vacuum. Using microwaves to sinter powder compacts offers reduced energy consumption and low "buy to use" ratio, and opens a new domain for making unique alloys that cannot be made by conventional processes.

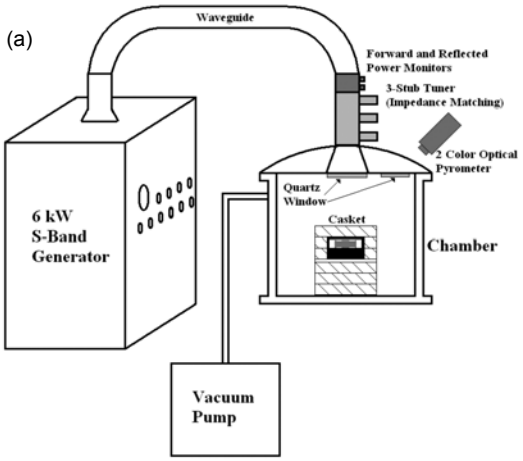

(b)

FIGURE 10
(a) Schematic and (b) photograph of the NRL 6 kW, 2.45 GHz microwave system for titanium sintering experiments.

Sintering Experiments: Sintering of titanium metal/alloy powder compacts has been carried out in our microwave materials processing system shown in Fig. 10. Microwaves are generated in a 6 kW, 2.45 GHz magnetron (Cober Electronics S6F Microwave Generator) and transported to the heating chamber via S-band waveguide. An impedance-matching three-stub tuner is used to optimize microwave transmission into the chamber. Typically, the coupling impedance drops during processing as the compact becomes more lossy at higher temperatures and the tuner must be constantly adjusted to minimize the reflected power. A liquid-nitrogen sorption pump, backed up by a mechanical vacuum pump, is connected to the chamber during the sintering process to minimize the risk of oxygen contamination.

Compacts of Ti powders were made by compressing commercially pure (CP) titanium and titanium alloy, Ti-6Al-4V, powders in a uniaxial or cold isostatic press (CIP). The CIP is of particular interest as it can achieve the highest pressures (up to 100 ksi) and is also capable of forming compacts with complex shapes. Scanning electron micrographs of typical select powders are shown in Fig. 11. The compacts were heated to peak temperatures of 900 to 1300 °C for hold times of 10 to 60 min. The only limiting factor for increasing the power was the formation of plasma in the chamber, which is generally unfavorable to work piece heating; however, plasma was no longer a problem after the sample had reached a temperature of ~600 °C. Above this temperature, the microwave coupling to the titanium compact is quite efficient and the microwave fields drop below the breakdown value. The surface temperature of the compact was measured with a two-color optical pyrometer. Figure 12(b) shows a powder compact of CP Ti cold isostatically pressed into the approximate shape of a small in-line valve body (Fig. 12(a) shows the original brass valve) and subsequently sintered at 1200 °C with a ramp rate of about 30 °C/min and a hold time of 30 min (Fig. 12(c)). To improve microwave heating efficiency during initial heating, lossy "susceptor" material consisting of a silicon carbide plate and zirconia fiberboard was added to the insulating casket; this technique is called hybrid heating. This

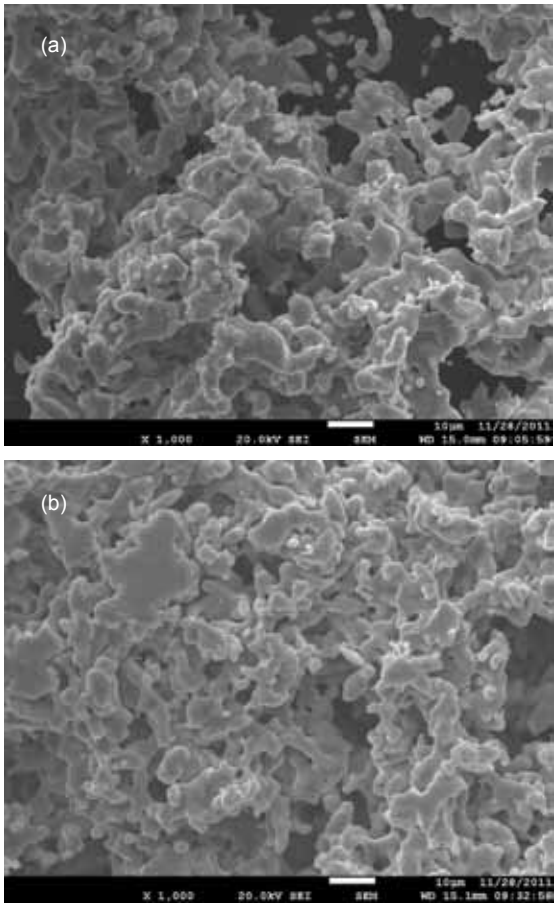

FIGURE 11
Scanning electron micrographs of powders of (a) commercially pure (CP) titanium and (b) titanium alloy, Ti-6Al-4V.

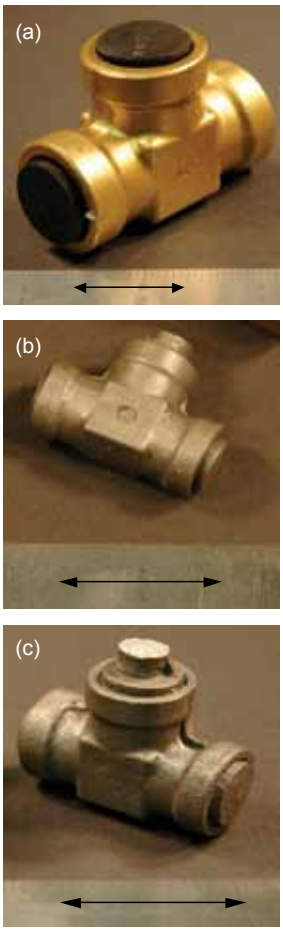

FIGURE 12
Photographs with 1-inch marker showing (a) original brass valve, (b) cold isostatically pressed Ti powder compact replicating the brass valve, and (c) sintered compact.

system provided better heating at subsintering temperatures and could be used repeatedly.

It was found that the compacts could be sintered to near theoretical density (TD) at temperatures ranging from 900 to 1300 °C. The alloy Ti-6Al-4V powders achieved 99% TD and the CP Ti powders achieved 98.5% TD. The results indicate that varying the hold time from 10 min to 60 min did not have a significant effect on the final density of the titanium, allowing for fast heating cycles. Experiments have shown that the powder type and the initial compaction pressure also affect the final density. Compaction pressure can be adjusted to achieve the desired final sintered density.

Summary: It is evident that microwave sintering is a potentially low-cost, energy-efficient process for processing powder metallic materials to near-net-shape parts. We believe the economics of microwave processing will be superior to any conventional process.[2] Research will continue to focus on controlling the final density, microstructure, and other properties of the sintered product.

[Sponsored by the NRL Base Program (CNR funded)]

References

[1] D. Lewis III, M.A. Imam, A.W. Fliflet, R.W. Bruce, L.K. Kurihara, A.K. Kinkead, M. Lombardi, and S.H. Gold, "Recent Advances in Microwave and Millimeter-Wave Processing of Materials," *Materials Science Forum* vols. 539–543, pp. 3249–3254 (2007), doi:10.4028/www.scientific.net/MSF.539–543.3249.

[2] R.W. Bruce, A.W. Fliflet, H.E. Huey, C. Stephenson, and M.A. Imam, "Microwave Sintering and Melting of Titanium Powder for Low-Cost Processing," *Key Engineering Materials* vol. 436, pp. 131–140 (2010), doi:10.4028/www.scientific.net/KEM.436.131.